ORIGINAL PAPER

Influence of the W and Ta content on the High-Temperature Oxidation Resistance of Multinary Co/Ni-Based Superalloys at 1050 °C and 1150 °C

S. P. Hagen[1] · L. Haussmann[2] · B. Wahlmann[3] · F. Gebhardt[1] ·
B. Abu-Khousa[1] · M. Weiser[2] · S. Neumeier[2] · C. Zenk[3] ·
Sannakaisa Virtanen[1]

© The Author(s) 2023

Abstract

Outstanding inherent environmental resistance is a precondition for the use of superalloys in high-temperature applications. Besides high Al and Cr levels, also refractory metal concentrations (W and Ta) are reported to affect protective scale formation, as these elements are expected to affect the chemical activity and also the transport of protective scale formers within the alloy. In this study, we elucidate the high-temperature oxidation behavior of 3 Co-based (Co/Ni ratio: 1.4) and 3 Ni-based (Co/Ni ratio: 0.7) superalloys differing in W and Ta levels. Time-resolved thermogravimetric analysis (TGA) in synthetic air at 1050 °C and 1150 °C for 100 h, scanning electron microscopy analysis (SEM), thermodynamic calculations using the CALPHAD software Thermo-Calc, and diffusion couple experiments were conducted to assess the impact of the Co/Ni ratio and the refractory metal content on the oxidation performance. The results indicate that a low W content (3 vs. 5 at.%) and a high Ta content (2.1 vs. 1.5 at.%) beneficially affect the oxidation resistance, as alumina scale formation is facilitated.

Keywords High-temperature oxidation · Cobalt-base superalloys · Protective scales · Refractory metals

Introduction

Single-crystalline (SX) Ni-base superalloys (SA) with γ/γ' microstructure can provide good mechanical capabilities and excellent resistance against high-temperature oxidation [1, 2]. Refractory metals like W, Re, Ta, Mo, and Ru contribute to solid solution and precipitation hardening in SAs, enabling superior mechanical properties at high temperatures [3, 4]. The concentrations of refractory metals have been

---

Extended author information available on the last page of the article

increased over the years (e.g., increasing Re content comparing first-, second-, and third-generation Ni-base superalloys), to max out the mechanical capabilities [5, 6]. Increasing the refractory metal content, however, is not a universal remedy for a general improvement, since undesirably high levels initiate TCP-phase formation [7]. Furthermore, a deterioration of the environmental resistance can be provoked too, as protective scale formation can be impeded [4, 8–11]. Ni-base SA are nowadays considered close to having reached their fundamental limits, meaning that new materials are desired [12]. Hence, the interest in γ'-hardened Co-base superalloys continuously grew over the past two decades [13]. So far, promising mechanical properties were clearly demonstrated for this comparably new class of material [14, 15]. However, the environmental capability of Co-base SA is still outmatched by Ni-base systems [16]. It remains a severe hurdle that the maximum Al and Cr levels in Co-base systems are strongly limited by the compositional range in which the desired γ/γ' microstructure is stable [14, 17–20]. Therefore, many γ/γ' Co-base superalloys are not capable to grow sustainable protective oxide scales of alumina or chromia via external oxidation within the high-temperature regime, and oxidation-resistant coatings are, therefore, developed [21, 22]. Co-base systems are prone to internal oxidation, meaning the nucleation of distinct alumina precipitates within the alloy when the solubility limit of oxygen is exceeded [23, 24]. Dependent on the system, the process of internal oxidation may continue, leading to a steadily penetrating internal oxidation zone (IOZ), which is made up of separated alumina precipitates, only [25]. This unwanted behavior is especially pronounced in the case of high oxygen inward fluxes or low Al-outward flux from the alloy [26, 27]. If a sufficient Al transport can be supplied by the substrate, counterbalancing the inward diffusing oxygen, already existing alumina precipitates can coarsen in the lateral direction. Ultimately, coarsening precipitates may coalesce and initiate a time-dependent transition to lateral continuous alumina subscale growth [25, 28–30]. In other words, this means a transition from internal to external oxidation may occur. This is described for binary alloys by the well-known Wagner criterion and less frequently applied for alloys with more elements [28]. Even though experimental verifications for the more complex compositions remained scarce, its qualitative meaning is undisputed [31] and acts as a working hypothesis for this study.

Recently [16], we elucidated the oxidation resistance of the multinary single-crystal Co-rich superalloys ERBOCo-1 [32] and ERBOCo-1X [33] up to 1050 °C in synthetic air. Both ERBOCo alloys contain identical levels of Al, Cr, W, Ta, Ti, Si, and Hf but different Co/Ni ratios (1.4 for ERBOCo-1 and 0.7 for ERBOCo-1X). The study [16] clearly identified a high Ni/Co-ratio to enhance the oxidation resistance (the mass gain after 100 h exposure at 1050 °C of ERBOCo-1 was factor ca. 2.1 higher than that of ERBOCo-1X). Elemental segregations could be identified to primarily account for the high mass gain of ERBOCo-1, since above-average oxide thicknesses were detected for dendritic regions (D). Qualitatively, this behavior prevails for both alloys; however, it was much stronger pronounced in the case of ERBOCo-1 compared to ERBOCo-1X. After 100 h at 1050 °C, for the interdendritic regions (ID) of both alloys comparably thin and laterally continuous protective scales (alumina underneath a chromia scale) were locally developed. In the case of D, however, massive internal alumina formation is reported, which cannot hinder

the growth of thick outer Co–Ni-oxide scales [16]. For both alloys, ERBOCo-1 and ERBOCo-1X, along D increased Co, Cr (sic!), and W contents prevail, whereas above-average levels of Ni, Al, Ti, Ta, Si, and Hf were found in ID [16]. It was concluded in [16] that increased W levels account for the deteriorated environmental resistance along D, as a high refractory metal content is reported to lower the diffusivity of protective scale formers like Cr, Al, and Si in the alloy (Wagner Criterion) [3, 34–40]. In the case of ID, above-average Ta contents were inferred to cause a beneficial effect on protective scale growth [16]. Truly, Ta is also a refractory metal and is as such sometimes also expected to lower the diffusivity of protective scale formers [3, 34, 35]. In this context, it is, however, noteworthy, that the interdiffusion constant of Ta itself outmatches the respective values of not only W but also Cr within Co (fcc) [41]. In addition, the large thermodynamic stability of Ta_2O_5 (more stable than chromia [42, 43]) may play an important role, too. This means that Ta might lower the inward oxygen flux and hence contribute to a faster transition from internal to external oxidation. This mechanism of secondary oxygen gettering (also referred to as the "third element effect") is well known in the case of ternary Ni–Al-Cr alloys [3, 44–48]. To check if our conclusions in [16] hold and if on their basis, the oxidation performance of ERBOCo-1 and ERBOCo-1X can be further optimized, new alloys (derivatives) differing in W and Ta levels were designed. In the case of W, decreasing its content was expected to be beneficial as thin scales were revealed for D regions [16]. In the case of Ta, derivatives of somewhat higher overall Ta contents should provide better environmental resistance [16]. Therefore, the W derivatives contain lower W levels and are denoted ERBOCo-1-W and ERBOCo-1X-W. The Ta derivatives possess higher Ta levels and are named ERBOCo-1 + Ta and ERBOCo-1X + Ta. In absolute values, the nominal change in W and Ta levels was set to 40% for the derivatives and was counterbalanced by the Co and Ni content while keeping the Co/Ni ratio of ERBOCo-1 and ERBOCo-1X constant.

In this study, firstly, the oxidation behavior of the SX derivatives is compared to the original alloys ERBOCo-1 and ERBOCo-1X at 1050 °C and 1150 °C using isothermal thermogravimetric analysis (TGA) and electron microscopy investigations. Secondly, thermodynamic calculations on the impact of the refractory metal levels on the chemical activity of Al, Cr, and Si are provided. Thirdly, diffusion couple experiments are performed using a binary Co/Ni single crystal and the SA ERBOCo-1, ERBOCo-1-W, and ERBOCo-1 + Ta in order to assess the influence of the W and Ta content on the diffusional transport of protective scale-forming elements Al and Cr within the alloys.

Experimental Procedures

Sample Materials

The multinary Co-base alloys ERBOCo-1, ERBOCo-1-W, ERBOCo-1 + Ta, and ERBOCo-1X, ERBOCo-1X-W, and ERBOCo-1X + Ta, as well as a binary Co/Ni ingot, were cast as single crystals (SX) with nominal < 001 > orientation along

Table 1 Nominal elemental compositions of the alloys in at.% as well as respective Co/Ni ratios [49]

Alloys	Co/Ni	Co	Ni	Al	Cr	W	Ti	Ta	Si	Hf
ERBOCo-1	1.39	44.50	32.00	8.00	6.00	5.00	2.50	1.50	0.40	0.10
ERBOCo-1-W	1.39	45.66	32.84	8.00	6.00	**3.00**	2.50	1.50	0.40	0.10
ERBOCo-1 + Ta	1.39	44.15	31.75	8.00	6.00	5.00	2.50	**2.10**	0.40	0.10
ERBOCo-1X	0.72	32.00	44.50	8.00	6.00	5.00	2.50	1.50	0.40	0.10
ERBOCo-1X-W	0.72	32.85	45.65	8.00	6.00	**3.00**	2.50	1.50	0.40	0.10
ERBOCo-1X + Ta	0.72	31.75	44.15	8.00	6.00	5.00	2.50	**2.10**	0.40	0.10
Binary Co/Ni	1.39	58.20	41.80							

The numbers in bold are important to guide the eyes of the reader and to allow a quicker recognition of the core-values

Table 2 Actual elemental compositions of the alloys in at.% as well as respective Co/Ni ratios, determined by ICP-OES in as-cast state [49]

Alloys	Co/Ni	Co	Ni	Al	Cr	W	Ti	Ta	Si	Hf
ERBOCo-1	1.39	45.01	32.45	7.86	5.90	4.99	2.12	1.4	0.18	0.09
ERBOCo-1-W	1.38	46.14	33.33	7.87	5.79	3.12	2.08	1.39	0.17	0.10
ERBOCo-1 + Ta	1.23	42.49	34.66	7.77	6.00	4.97	2.09	1.72	0.21	0.09
ERBOCo-1X	0.71	32.34	45.42	7.72	5.93	4.85	2.07	1.37	0.20	0.09
ERBOCo-1X-W	0.73	33.78	46.19	7.70	5.68	2.95	2.06	1.36	0.20	0.09
ERBOCo-1X + Ta	0.67	30.94	46.11	7.80	5.95	4.87	2.08	1.92	0.23	0.10

Measurement uncertainties are ± 0.15 for Co and Ni, ± 0.05 for Al, ± 0.07 for W, ± 0.03 for Ti, ± 0.05 for Cr, ± 0.05 for Ta, ± 0.02 for Hf, and ± 0.005 for Si at most

the rod-axis (12 mm diameter). For this Bridgeman investment casting (by the Institute of Metals Science and Technology (WTM, University of Erlangen-Nürnberg (FAU), Germany) was performed. The exact compositions were investigated using inductively coupled plasma optical emission spectrometry (ICP-OES) in the as-cast state (Institut für Materialprüfung Glörfeld GmbH, Germany). To save single-crystalline material for the ICP-OES investigations, samples were taken from the polycrystalline starter block of the ingots (right below the grain selector). The nominal and the measured elemental levels are provided in Tables 1 and 2, respectively.

In this study, all ERBOCo alloys were used in heat-treated state, according to a heat treatment of short duration (HTS) [16] initially introduced by Volz et al. [32]. A solution annealing step of a duration of 8 h at 1280 °C was followed by aging treatment for 5 h at 1050 °C and a final period of 16 h at 900 °C. For the diffusion couple experiments, the 16 h heat-treatment step at 900 °C was skipped for both the binary Co/Ni-samples and the superalloys. Figure 1 indicates the two-phase microstructure of the superalloys at dendrite core positions. One can see that the γ'-volume fraction of the W derivatives (Fig. 1c and f) is reduced compared to the original alloys (Fig. 1a and d) and the Ta derivatives (Fig. 1b and e).
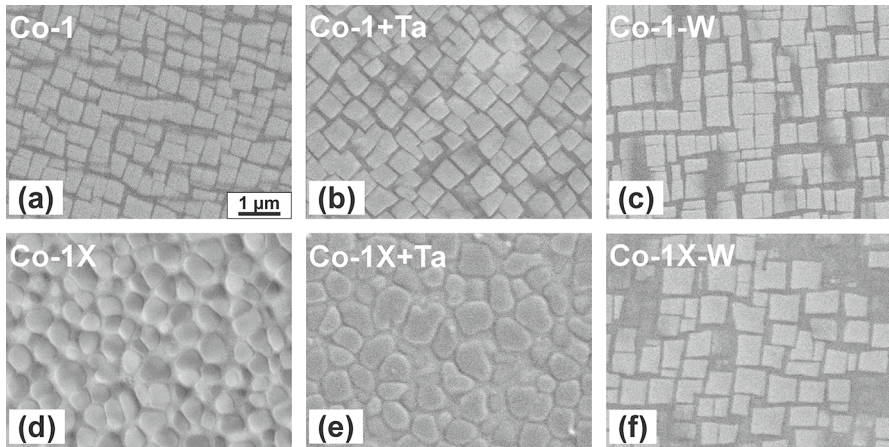
Fig. 1 Representative BSE micrographs of investigated alloys, with **a** for ERBOCo-1, **b** for ERBOCo-1 + Ta, **c** for ERBOCo-1-W, **d** for ERBOCo-1X, **e** for ERBOCo-1X + Ta, and **f** for ERBOCo-1X-W

Oxidation

Continuous thermogravimetry was conducted in a SETSYS Evolution 1650 TGA from Setaram for 100 h in synthetic air (20% O_2, 80% N_2 from Linde) at 1050 °C. Heating and cooling rates of 5 K/min were used for these experiments. Gas flow was set to 20 ml/min, equaling 7.86 cm/min within the furnace when laminar flow conditions are assumed. Taring of the balance was conducted prior to heating. Samples with a thickness of 1 mm were cut from the SX rods for the oxidation experiments. After grinding, polishing was conducted with diamond suspensions with a final step at 1 μm. Details on sample preparation remained unaltered from our recent study [16], to assure good comparability.

Diffusion Couples

Overall, three diffusion couples were manufactured. One side consisted of the binary single-crystal Co/Ni alloy, and the other side was either out of ERBOCo-1, ERBOCo-1-W, or ERBOCo-1 + Ta, respectively. For the diffusion couple experiments, samples of a thickness of 2 mm were cut from the SX rods and subsequently cut in half, leading to half-rounded pieces. These samples were polished down to 1 μm grit size just as for the oxidation experiments. Additionally, electropolishing at 100 V in Electrolyte A3 from Struers was performed to guarantee a defect-poor surface. To join the alloys, a molybdenum-based holder was used that allowed the clamping of the nominal 100-faces of the two alloy pieces on each other by means of a hexagon socket screw. To prevent joining the samples with the molybdenum screws during exposure, thin aluminum oxide ceramic plates were placed in between. The diffusion couples were then annealed in a vacuum furnace from Nabertherm (model: RHTC 80–450) at 1050 °C for 250 h using heating and cooling

rates of 5 K/min. After reaching the target temperature, the attached turbomolecular pump operated at a pressure below 5×10^{-5} mbar.

Microscopic Characterization

To clearly depict the initial two-phase microstructure of the alloys, (flat) ion milling of the mechanically pre-polished samples using a 75° incidence angle was conducted (using an IM4000 from Hitachi). Subsequently, a scanning electron microscope (SEM) (Tescan LYRA3), equipped with a backscattered electron (BSE) detector, was used. After exposure, Ni plating was performed in order to prevent scale spallation during the metallurgical preparation of cross sections. Therefore, first, a thin electrically conductive Au-layer was applied by sputtering. Afterward, galvanostatic Ni plating was performed using a NiSO4-based solution [16]. After Ni plating, the samples were cut in half using a low-speed saw. Finally, cross-sectional ion milling was conducted to obtain high-quality cross sections. The SEM micrographs were again taken using a Tescan LYRA3 microscope. To record the elemental distribution in the case of the diffusion couples line scans were taken by electron probe microanalysis (EPMA) using a JEOL JXA-8100.

Results

Oxidation Behavior

TGA-based investigations (Fig. 2) for 100 h duration were conducted. Figure 2a (Co-base alloys) and Fig. 2b (Ni-base alloys) show the results for exposure at 1050 °C. The original alloy ERBOCo-1 exhibits high oxidation kinetics. The final mass gains of both derivatives, ERBOCo-1 + Ta (0.88 mg/cm^2) and ERBOCo-1-W (1.56 mg/cm^2) are significantly lower than for the original alloy ERBOCo-1 (4.00 mg/cm^2). Also, for the Ni-base alloys (Fig. 2b), it can be seen that both lowering the W-level and increasing the Ta content leads to slower oxidation kinetics. Just as for the Co-based alloys, the Ta-derivative ERBOCo-1X + Ta revealed the highest oxidation resistance (0.83 mg/cm^2). Additionally, the overall mass gain of ERBOCo-1X-W (1.11 mg/cm^2) clearly stays below the respective counterpart, ERBOCo-1X (1.77 mg/cm^2). Comparing Fig. 2a and b, the highest oxidation resistance is recorded in the case of the Ta derivatives. In addition, the overall mass gain of W derivatives remains below the one of the original alloys. To confirm if the revealed impacts persist at higher temperatures, additional experiments were conducted. At 1150 °C (Fig. 2c), again a reduction of the W content as well as an increase in Ta content increased the oxidation resistance. At 1150 °C, overall mass gains of 12.4 mg/cm^2, 5.27 mg/cm^2, and 1.80 mg/cm^2 were recorded for ERBOCo-1, ERBOCo-1-W, and ERBOCo-1 + Ta, respectively. The same trend was also found for the Ni-base systems (Fig. 2d). In numbers, the mass gain of 7.97 mg/cm^2 for ERBOCo-1X compares with 5.30 mg/cm^2 for ERBOCo-1-W and 1.76 mg/cm^2 for ERBOCo-1X + Ta. Despite significant improvement via
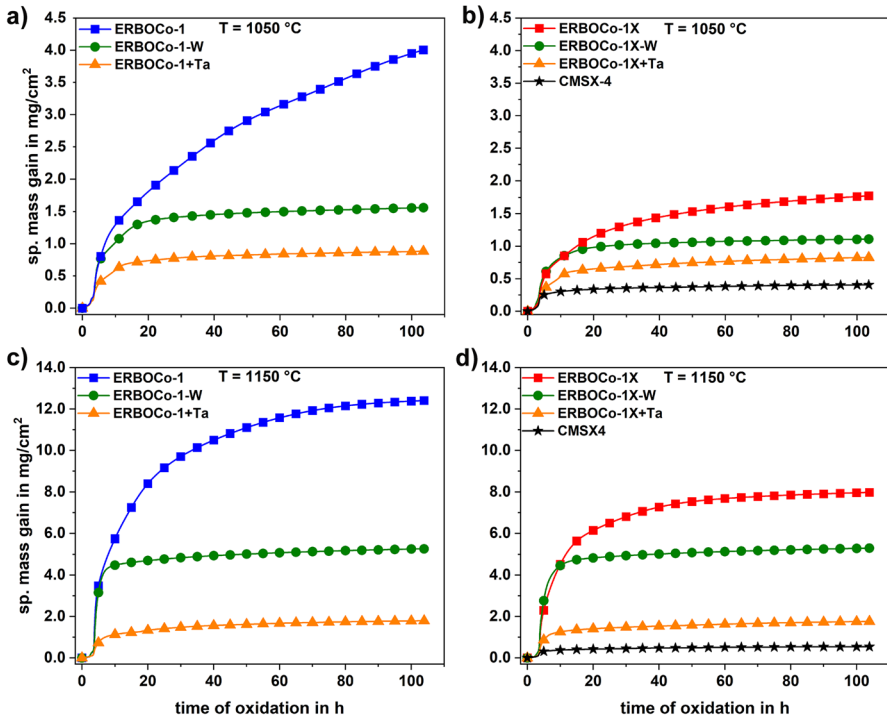
Fig. 2 Continuous specific mass-gain curves, recorded during isothermal oxidation for 100 h. Graphs **a** and **b** represent the outcome for Co- and Ni-base alloys at 1050 °C, respectively, whereas **c** and **d** refer to 1150 °C. In addition, the respective results for CMSX-4 (samples material taken from study [16]) are also provided in (**b**) and (**d**)

derivatization, it has to be stated that none of the ERBOCo alloys reach the oxidation resistance of commercial CMSX-4 at 1050 °C (0.45 mg/cm^2) and 1150 °C (0.54 mg/cm^2). Representative top views (SE) micrographs are evaluated to elucidate if segregation during castings correlates with the oxide growth. The dendrite cores of the original alloys ERBOCo-1 and ERBOCo-1X were clearly identified to exhibit enhanced oxide thicknesses after exposure at 1050 °C [16]. Consequently, the dendrite shape can still slightly be recognized in the oxide topography shown in Fig. 3a and d. The surface oxides of the derivatives differ from that of the original alloys. The surfaces of samples with reduced W or increased Ta content (Fig. 3b, e, c, and f) are dominated by oxide nodules that appear randomly distributed. Definitely, neither positions nor spatial extension could be correlated to the dendritic structure by means of electron microscope images, only.

To provide an insight into the scale structure after exposure for 100 h at 1050 °C, cross sections were prepared for the Co-base (Fig. 4) and the Ni-base alloys (Fig. 5). In order to account for the above-described inhomogeneous nature of oxidation, both regions of extensive scale growth (referred to as "thick") and protective behavior that result in thin oxide scales are shown. In Ref. [16, 49]
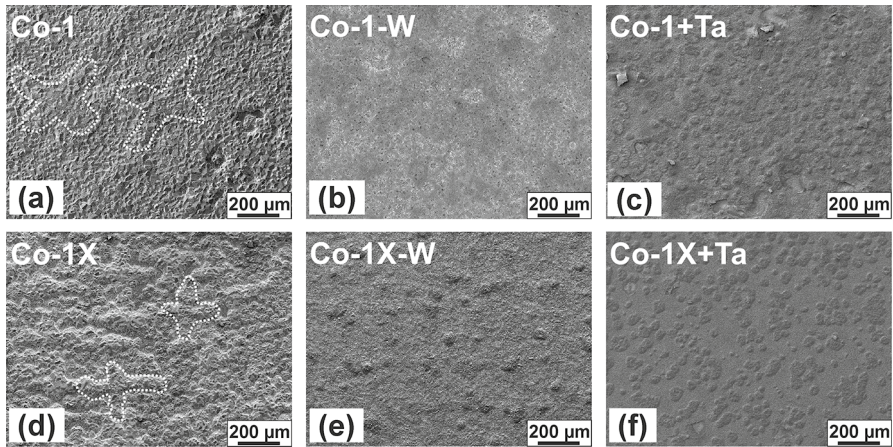
Fig. 3 Representative SE-micrographs of the oxidized alloy surfaces after exposure at 1050 °C for 100 h. The upper row **a**, **b**, and **c** refer to the Co-base SA ERBOCo-1, ERBOCo-1-W, and ERBOCo-1+Ta, respectively. The lower row **d**, **e**, and **f** show the surfaces of the Ni-base SA ERBOCo-1X, ERBOCo-1X-W, and ERBOCo-1X+Ta, respectively. Exemplarily the dendrite shape is highlighted in (**a**) and (**d**)
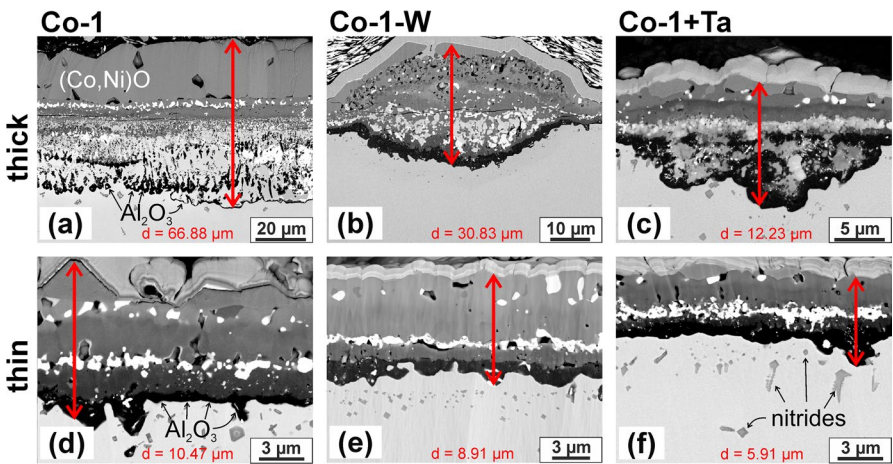

Fig. 4 BSE micrographs of thick (**a**, **b**, and **c**) and thin (**d**, **e**, and **f**) oxide spots of the Co-base SA ERBOCo-1 (**a** and **d**), ERBOCo-1-W (**b** and **e**), and ERBOCo-1+Ta (**c** and **f**) after exposure at 1050 °C for 100 h. The spots of the maximum thicknesses are marked by red arrows. The respective thickness values d are provided within each micrograph

information regarding the chemical composition of individual oxide phases and layers is provided for ERBOCo-1 and ERBOCo-1X. The external scale was demonstrated to consist of (Co,Ni)O; beneath W, Ta, and Cr oxides were found. Moreover, alumina was verified to grow at the internal oxidation front [16, 49]. Due to the pronounced morphological similarity among the cross sections, it is expected that these results qualitatively also apply to the derivatives of this study. Knowing
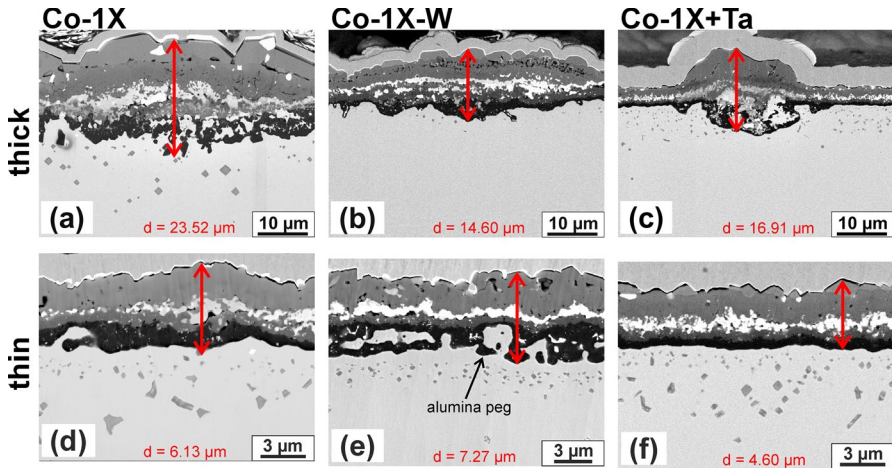
Fig. 5 BSE micrographs of thick (a, b, and c) and thin (d, e, and f) oxide spots of the Ni-base SA ERBOCo-1X (**a** and **d**), ERBOCo-1X-W (**b** and **e**), and ERBOCo-1X + Ta (**c** and **f**) after exposure at 1050 °C for 100 h. The spots of the maximum thicknesses are marked by red arrows. The respective thickness values d are provided within each micrograph

that the BSE contrast correlates to the atomic mass and knowing that alumina is the lightest oxide that can form, the darkest phase within the cross sections can be concluded to be alumina even without further verification (also frequent observations of the oxidation community nurture this argument) [50–52].

The original alloys ERBOCo-1 (Fig. 4a) and ERBOCo-1X (Fig. 5a) demonstrate thick multilayered oxide scales [16]. For both compositions, discrete internal alumina precipitates formed at the internal oxidation front (IOF). In contrast, the thin spots (Figs. 4d and 5d) demonstrate a continuous alumina scale at the oxide/alloy interface. Elemental distribution maps of the oxide scales can be found in Fig. 11. The positions of the dendrite cores align with the position of the thick spots, whereas the interdendritic regions match the thin spots. Comparing ERBOCo-1 and ERBOCo-1X to their respective derivatives, it is noteworthy that the oxide thicknesses among the thin spots exhibit similar values. The largest difference of approximately 6 μm can be found comparing Fig. 4d (ERBOCo-1) and Fig. 5f (ERBOCo-1X + Ta). This is, as according to Refs. [16, 49] locally continuous scales of alumina and chromia grow in the case of the original alloys. Due to the pronounced morphological similarity among the thin scale spots (d, e, and f in Figs. 4 and 5), the latter are expected to grow also in the case of the derivatives.

In contrast, the thick spots strongly differ, as among these in the case of the derivatives much thinner scales are on hand than for the original alloys. In the case of Co-base alloys, this means a thickness reduction from 66.88 μm (Fig. 4a, ERBOCo-1) to 30.83 μm (Fig. 4b, ERBOCo-1-W) or to 12.23 μm (Fig. 4c, ERBOCo-1 + Ta), respectively. In the case of the Ni-base alloys, the oxide thickness at the thick spots was lowered from 23.52 (Fig. 5a, ERBOCo-1X) to 16.91 μm (Fig. 5c, ERBOCo-1X + Ta) to 14.60 μm (Fig. 5b, ERBOCo-1X-W). Most interestingly, in the case of ERBOCo-1X + Ta (Fig. 5c and f), the alumina scales demonstrate a highly uniform

and homogeneous appearance. Overall, all derivatives exhibit significantly smaller differences between the thicknesses of multilayered oxide scales comparing thick and thin regions. This is supported by the finding of thin and apparently continuous alumina layers that terminate the overall thicker oxide scale regions at the IOF. In other words, the rapid inward flux of reactive species (O/N) is effectively hindered, even though these alumina layers can be prone to different degrees of peg formation and warping (see Fig. 5e). In contrast, for the original alloys, the massive persistent scale growth along the dendrite cores due to internal alumina formation was identified to account for the very high mass-gain rates [16].

It is well known that selective oxidation can lead to the dissolution of the γ' phase in surface proximity [53]. In the case of W derivatives, the thickest γ'-depleted zone developed. In contrast, the original compositions and especially the Ta derivatives were less prone to γ' dissolution. Since the intention of the micrographs was to depict the oxide scale, the selected magnification or contrast parameters do not allow one to recognize the γ'-dissolution zone. The latter can be recognized in Fig. 10 within the appendix part of this work.

After oxidation at 1150 °C, the external oxide scales of Co-based alloys spalled during cooling due to thermal mismatch stresses. Figure 6 shows the remaining cross sections of the three considered alloys. For ERBOCo-1, the penetration depth of the internal oxidation front varies strongly in the displayed region (Fig. 6a). Similar to oxide scale growth at 1050 °C, sections of deep internal oxidation preferentially formed at dendritic regions. All sample surfaces were of planar shape prior to exposure. Therefore, it can be concluded that in the case of ERBOCo-1-W (Fig. 6b) and ERBOCo-1 + Ta (Fig. 6c), the detected internal alumina layer formed at an early stage and slowed down further internal oxidation. The oxidation behavior of derivatives appears mostly unaffected by the dendritic microstructure.

Calculation of Chemical Activities of Al, Cr, and Si in Dependence on Alloy Composition

In order to estimate the driving force for initial oxide nucleation, chemical activities of Al, Cr, and Si are of crucial importance. Therefore, the impact of the derivatization (lowering the W content and increasing the Ta content by 40%, each) on the chemical activities a_{Al}, a_{Cr}, and a_{Si} was elucidated for all alloys. For the ERBOCo
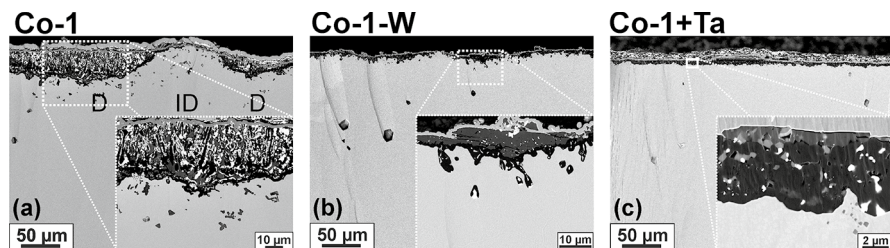

Fig. 6 BSE micrographs of the Co-base SA ERBOCo-1 (**a**), ERBOCo-1-W (**b**), and ERBOCo-1 + Ta (**c**) after exposure at 1150 °C for 100 h

alloys, the respective values between 950 and 1250 °C were calculated based on the actual composition (determined via ICP-OES, see Table 2) using Thermo-Calc and the TCNI10 database. For CMSX-4, the nominal composition given in Ref. [16] was used since no precise ICP-OES data was available. Regarding the Al and Si activities of the ERBOCo alloys, Fig. 7a and c indicates that overall higher activities of elements are present in the Co-based systems compared to their Ni-based counterparts. The Ta derivatives surpass the original composition in activity, whereas the W derivatives show reduced values. This is inconsistent with the TGA data for mass gain. Residual segregation could be a possible explanation for this. In Zenk et al. [33], we had already shown that the W-concentrations after standard heat treatment in regions ID and D can still range from ~ 12 to 16.5 wt.% (4.1–5.8 at.%). Further studies are required to isolate the influence of residual segregation on the local oxidation behavior. Overall, higher activity values for Al than for Si were determined. This reflects the different elemental levels within the alloys. Regarding the Cr activities (see Fig. 7b), it is noteworthy that overall significantly higher values are on hand than for Al. The latter is interesting as the Al concentrations (in at. %) in the ERBOCo alloys are higher than those of Cr. Moreover, the Cr activities of all alloys decrease with increase in temperature, which is the opposite kind of behavior compared to what is on hand for Al and Si. Similar to the variations of the Al and the Si activity, increasing the Ta content leads to increased Cr activities for both
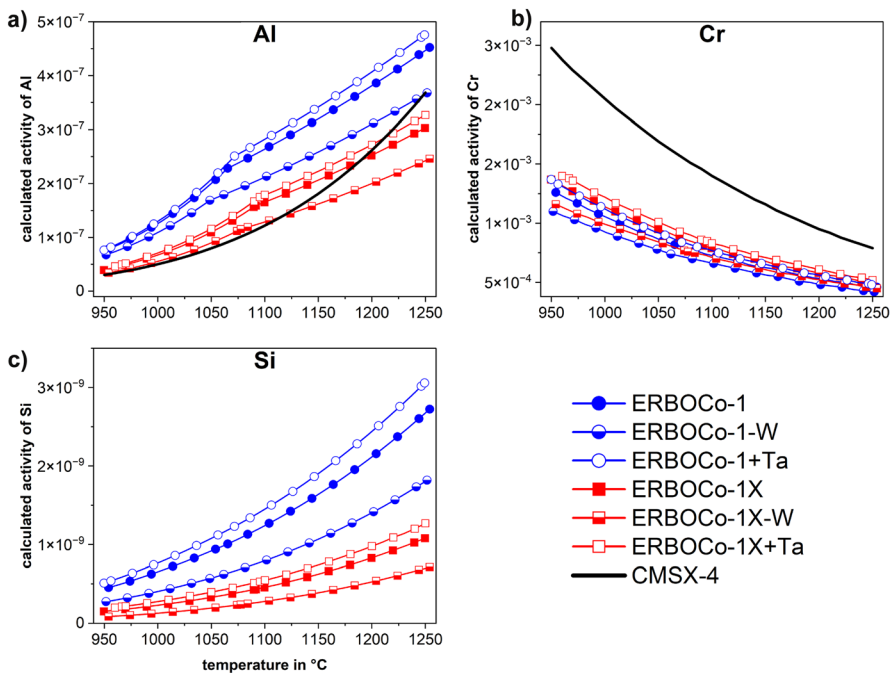

Fig. 7 Chemical activities of Al (**a**), Cr (**b**), and Si (**c**) over temperature, calculated using Thermo-Calc and the TCNI10 database. For all ERBOCo alloys, the actual composition determined via ICP-OES (see Table 2) was used for calculation, whereas in the case of CMSX-4 the nominal composition given in [16] was used

the Co-base and the Ni-base alloys. As expected, the decrease of W results in an opposite trend, namely lowered Cr activities. Compared to Al and/or Si, the variation of Cr activities with alloy composition appears more complex. Each Ni-base alloy (ERBOCo-1X, ERBOCo-1X-W, and ERBOCo-1X + Ta) demonstrates higher Cr activities compared to their respective Co-base system. In the case of CMSX-4, it is noteworthy that the Al activity is comparably small (and similar to the Ni-base ERBOCo alloys) within the considered temperature regime (below 1150 °C). At higher temperatures, the slope of the curve increases and approaches the values of the Co-base compositions. The Cr activity for CMSX-4 clearly surpasses the values of all ERBOCo alloys.

Diffusion Couples

Diffusion couple experiments were conducted to elucidate to what extent the availability of protective scale-forming elements, i.e., Al, Cr, or Si, varies among the alloys ERBOCo-1, ERBOCo-1-W, and ERBOCo-1 + Ta. Therefore, 3 diffusion couples were manufactured using a binary Co/Ni single crystal with a Co/Ni ratio being equal to the respective nominal value of the 3 superalloys (see Table 1). Exposure was conducted for 250 h at 1050 °C. The concentration profiles of Al, Cr, and Si are depicted, comparing the 3 superalloys in each diagram. The position $x = 0$ μm defines the initial interface of each couple. At $x > 0$ the SA and at $x < 0$ the (initially) binary crystal is located. Since ERBOCo-1, ERBOCo-1-W, and ERBOCo-1 + Ta contain identical mole fractions of protective scale-forming elements, the release rates of the latter determine the elemental levels of Al, Cr, and Si on the Co–Ni side of the diffusion couples after exposure. Figure 8 demonstrates highly comparable elemental EPMA line scans across the ERBOCo-1- and ERBOCo-1 + Ta-diffusion couple. In the case of the ERBOCo-1-W-diffusion couple, however, the prevailing Al, Cr, and Si levels at $x < 0$ are larger than the respective values achieved with ERBOCo-1 and ERBOCo-1 + Ta. Notably, the concentration profiles indicate downhill diffusion of Al and Cr for all three alloys. The low bulk concentration values of Si (determined by ICP-OES and EPMA) make an unambiguous statement on the Si diffusion characteristics difficult. Furthermore, one can recognize that at values $x > 0$ even elemental distributions undergo a sudden transition toward a highly unsteady signal. The reason for the latter is the depletion-induced decay of the two-phase γ/γ' microstructure that can be recognized in Fig. 9. Obviously, ERBOCo-1-W shows the strongest γ' dissolution (γ'-free zone of 70.3 μm thickness, see Fig. 9b), whereas, in the case of ERBOCo-1 (Fig. 9a) and ERBOCo-1 + Ta (Fig. 9c), this effect is less pronounced (γ'-free zones of lower thicknesses; 48.9 μm and 47.2 μm, respectively).

Discussion

The present study indicates a lower oxidation resistance of the SA ERBOCo-1 and ERBOCo-1X at 1050 °C compared with the commercial SA CMSX-4. Especially in dendritic regions, massive internal oxidation (formation of distinct alumina
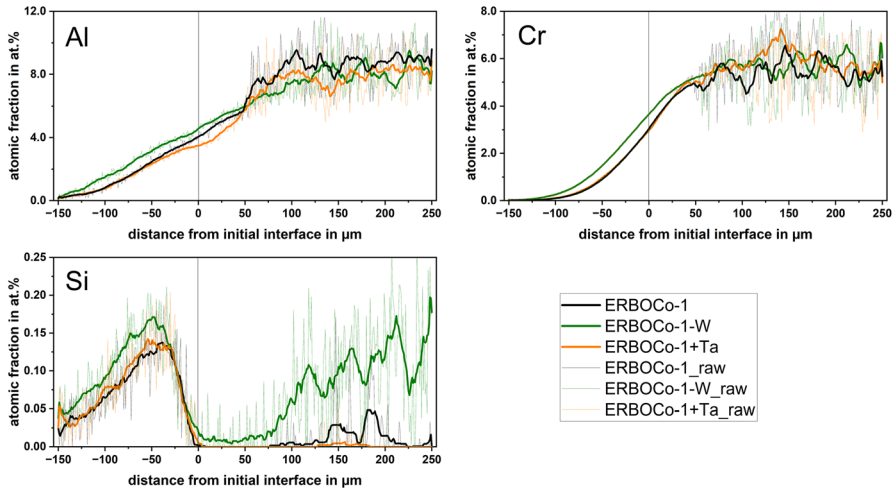
Fig. 8 EPMA line scan diagrams comparing the distribution of the protective scale formers (Al, Cr, and Si) in the orthogonal direction toward the interface of the diffusion couples (58,2Co-41,8Ni and one of the Co-base SA ERBOCo-1, ERBOCo-1-W, or ERBOCo-1+Ta) after exposure at 1050 °C for 250 h. The position of the initial interface is indicated via a vertical line (at position 0 μm). The binary side alloy is allocated at negative X-values
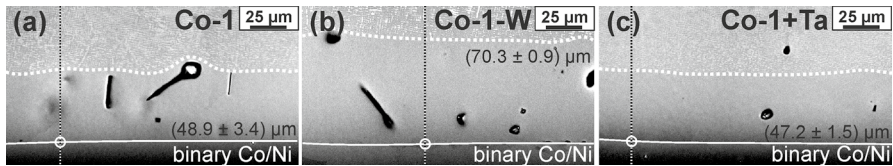

Fig. 9 BSE micrographs of diffusion couple cross sections after 250 h at 1050 °C. All micrographs are aligned equally, meaning the SA-part (ERBOCo-1 (**a**), ERBOCo-1-W (**b**), or ERBOCo-1+Ta (**c**)) is at the top, whereas the binary Co/Al alloy is at the bottom. The interface of the diffusion couples is highlighted by the lower white lines. Together with the horizontal dotted upper white line, the zone at which the γ' phase dissolved is noteworthy. The width of the latter is provided within each micrograph. The vertical dotted lines highlight the position of the line scans (dendrite cores). The position x=0 in Fig. 8 is marked using white circles within each of these diagrams

precipitates) for ERBOCo-1 and ERBOCo-1X is accompanied by growth of thick external non-protective oxide scales of (Co,Ni)O during exposure. In contrast, in the case of CMSX-4 a continuous alumina scale developed globally. This accounts for the significantly higher mass gains of ERBOCo-1 and ERBOCo-1X (Fig. 2). At the interdendritic regions, however, oxide scales with comparable thickness to CMSX-4 were found for ERBOCo-1, and ERBOCo-1X. This can be explained by a rapid formation of continuous alumina scales in all alloys that effectively protect the subjacent substrate. Both increasing the Ta content (ERBOCo-1/1X+Ta) and reducing the W content (ERBOCo-1/1X-W) strongly lower the overall oxidation kinetics at 1050 °C and 1150 °C as Fig. 2 indicates. This is because the persistent internal

formation of distinct alumina precipitates is avoided in the case of the derivatives. Even if internal oxidation that results in above-average oxidation rates locally prevailed (Fig. 4b and c, as well as Fig. 5b and c), thin continuous alumina subscales globally formed over time. Due to the continuity of the alumina subscales at later stages, the oxidation kinetics ultimately level out. The mechanisms through which oxidation resistance is affected by refractory metals are intricate and not totally understood [54]. Literature studies systematically addressing this topic are rare [55]. It is generally accepted that high levels of W, Re, Ru, and Mo lead to poor environmental stability [4, 8, 9]. In some cases, and especially for Ta, beneficial impacts on protective scale growth are reported, too [44, 45, 56, 57]. Considering the early stages of exposure, or more specifically the nucleation of oxide phases, thermodynamic driving forces can be expected to determine oxide formation. For the subsequent growth also the shape of these internal oxide precipitates and elemental transport along the respective alloy/oxide interfaces are crucial [58]. According to the law of mass action (Eq. 1), the Al activity a_{Al} (same considerations apply for Cr) affects the equilibrium constant K of the reaction. As Eq. 2 indicates, also the driving force for alumina formation ΔG (Gibbs free energy) is a function of a_{Al} as well as $\Delta G°$ the standard Gibbs free energy of formation, T the temperature, and R the gas constant.

$$K = \frac{a(Al_2O_3)^2}{a(Al)^4 * a(O_2)^3} \tag{1}$$

$$\Delta G = \Delta G° + RT \ln K \tag{2}$$

Knowing that negative values of $\Delta G°$ prevail, increasing a_{Al} hence means a reduction of K which ultimately is reflected in more negative ΔG values. According to Ref. [59], a high activity of protective scale formers should be favorable for protective scale growth. Even though the Al, Cr, and Si contents remained almost constant according to Table 2, thermodynamic predictions in Fig. 7 indicate that the activities were affected via derivatization: In the case of the Ta derivatives, the activities of Al, Cr, and Si increased, whereas in the case of the W derivatives, a decrease was effectuated. These results are in line with a recent study from Galiullin et al. that reported enlarged activities of Al and Cr coinciding with high levels of W and Ta in the alloy [57]. This means that during initial exposure, the Ta derivatives should have the highest thermodynamic driving force for the formation of alumina and chromia. In contrast, the W derivatives should have the lowest tendency. Therefore, protective oxide formation should be most pronounced for ERBOCo-1 + Ta, followed by the original alloy, and finally by ERBOCo-1-W, being worst. Obviously, the activity calculations cannot explain the oxidation resistance that was determined by TGA for the ERBOCo alloys. In the case of CMSX-4, the Cr activity clearly outmatches the values of all other alloys, in particular the one of the Ta derivatives. The early formation of chromia, therefore, significantly contributes to the superior oxidation performance of CMSX-4. It needs to be stated that in isolation the results on the activity of protective scale formers do not hold to explain the enhanced oxidation resistance of ERBOCo-1-W and ERBOCo-1X-W compared to the original alloys.

According to Wagner, after initial nucleation of distinct alumina or chromia particles (internal oxidation) the growth behavior is governed by diffusional fluxes: (i) the outward flux of, e.g., Al, Cr, and Si as well as (ii) the inward flux of oxygen within the alloy. A high outward flux of protective scale formers is beneficial since it contributes to the fast coarsening of individual oxide particles to ultimately form a continuous subscale. In contrast, the inward flux of oxygen should be low, in order to prevent a rapid penetration of the internal oxidation zone. To compare the extent to which the SA ERBOCo-1, ERBOCo-1-W, and ERBOCo-1 + Ta are able to release Al, Cr, and Si toward the surface, diffusion couples consisting of a binary SX Co/Ni alloy with identical base element ratio as the respective superalloys on the other side were manufactured. According to Wagner [28], the following can be taken as the working hypothesis: *The higher the released amount of protective scale formers, the better the oxidation resistance*. Therefore, high levels of Al, Cr, and Si on the initially binary side of the diffusion couples are interpreted as beneficial for an early growth of a continuous protective oxide scale that lead to improved oxidation performance. It is noteworthy that according to Table 2, the concentration of Al, Cr, and Si is at almost equal magnitudes. In general, refractory metals [3, 34, 35] but especially high W levels [36–40] were reported to decelerate the diffusional transport of protective scale formers in the alloy. If the provided literature holds, the ability for protective scale formation can be expected to be decreased in the case of ERBOCo-1 + Ta and increased in the case of ERBOCo-1-W. According to Fig. 8, a reduction in W-concentration is indeed accompanied by an increased release of Al, Cr, and Si and this outcome coincides with the TGA results (Fig. 2) according to Wagner. According to Fig. 2, besides a lower final mass gain it is especially noteworthy that for ERBOCo-1-W parabolic kinetics appear to establish quicker than for the original alloy composition (ERBOCo-1). It is concluded that at the D regions, alumina formation becomes rate controlling as soon as lateral continuity has been developed. The overall oxidation kinetics measured by TGA, therefore, reflect the individual time-dependent rates of ID and D regions (weighted by the respective surface fraction). However in the case of the Ta derivative, no distinct difference toward ERBOCo-1 regarding the protective scale former levels on the initial binary side of the diffusion couples is observed. This might be because diffusion-related transport is dependent on the overall composition but can also be affected by γ/γ' microstructure. Diffusivities within the intermetallic γ' particles can be up to 2 orders of magnitude lower than within γ [57]. Since the γ'-volume fraction is a function of the overall W and Ta concentration, a distinct impact on diffusional transport from the microstructure itself will follow [57]. Figure 1 clearly shows that the W derivatives have lower γ'-volume fractions, meaning that diffusion toward the binary side (or the oxide scale) should be facilitated. In contrast, the higher γ'-volume fraction might contribute to the similar (and lower) availability of protective scale formers in the case of ERBOCo-1 and ERBOCo-1 + Ta. Furthermore, decreasing the W content destabilizes the γ' phase, whereas Ta additions will stabilize the hardening phase. Knowing that Al is partially bound within the γ' phase, early dissolution of γ′ can be seen as a precondition for high Al-outward fluxes. Indeed, the width of the γ '-free zone in the case of the ERBOCo-1-W-diffusion couple (70.3 μm, see

Fig. 9b) is considerably larger than in the case of the ERBOCo-1- (48.9 μm, see Fig. 9a) and ERBOCo-1 + Ta-counterpart (47.2 μm, see Fig. 9c). In case of the W derivatives, the enhanced growth of continuous protective oxide layers can be explained by the supply of elements. Even though the chemical activity (driving force for diffusion) was lowered through the derivatization, increased outward diffusion is a more powerful influence. The latter might be a consequence of the lowered γ' volume fraction. Overall, the diffusion and oxidation results on the W derivatives confirm various studies, concluding a decelerating effect of high W levels on the transport of protective scale formers in the alloy [36–38, 51, 60, 61].

The reason why the Ta derivatives provide an improved oxidation resistance might not only be a consequence of the increase in protective scale former activities. Instead, the high oxygen affinity of Ta might also trigger the formation of protective scales [3, 44, 45]. This is because, through the formation of Ta-containing oxides, inward diffusing oxygen can be partially trapped. This trapping leads to a reduction of the residual oxygen inward flux (secondary oxygen gettering, as described for the third element effect) [46–48]. In Ref. [16, 49], the formation of Ta-containing oxide layers was demonstrated for ERBOCo-1 and ERBOCo-1X. In earlier investigations [49], the composition of oxide phases forming during the early stages of oxidation (2 min @1050 °C) of ERBOCo-1 directly below the Cr_2O_3 oxide scale was determined using STEM-EDX analyses [49]. Besides O, the main contributions were Ti (13.05 at.%) and Ta (9.83 at.%). The layer appears to be inhomogeneous. Due to the limited resolution of the STEM results, one cannot be sure if it is composed of Ta-containing spinel or of a mixture conglomerate of individual oxide grains phases of "pure" oxides (Ta_2O_5, TiO_2,… and others). Previous studies from the literature suggest that also the growth of a $TiTaO_4$ could form below the Cr_2O_3 layer [62–64]. This is in accordance with EPMA distribution maps in Fig.11. It can be seen that Ta-rich oxide layer separating alumina and chromia also reveals above-average contents of W and Ti. Knowing that this Ta-rich layer grows below the dissociation pressure of chromia one can conclude that it provides a certain degree of oxygen gettering for subjacent alumina formation. Irving et al. describe Ta additions of 1.2 at.%, 2.3 at.%, and 3.2 at.% to improve the oxidation resistance at 900 °C, 1000 °C, and 1100 °C for the Co-22Cr system due to this mechanism [44]. In the case of a Ni-base SA (Ni-4.2Co-4.8Cr-12.8Al-1.6W-3.1Mo-1.0Re), the addition of 1 at.% Ta was also found to positively affect oxidation resistance at 1000 °C and 1100 °C, whereas an addition of 3 at.% was identified to induce a deterioration [56]. Secondary oxygen gettering in the case of W might be less pronounced due to a considerably lower oxygen affinity: Considering the oxidation of pure elements at 1050 °C, a dissociation pressure of 4.4×10^{-14} atm for Ta_2O_5 compared with a value of only 5.76×10^{-24} atm for WO_3 can be determined [43].

The influence of refractory metals on oxidation resistance is highly complex and the impact of alloy composition on the grain structure of oxide scales and their defect chemistry was not investigated within this study, even though it is well known

to have an effect on oxidation kinetics [2]. However, it is emphasized again that the major improvement in oxidation resistance of the ERBOCo derivatives compared to ERBOCo-1/1X is due to the growth of a continuous protective subscale that suppresses massive oxidation kinetics. Therefore, effects determining the defect chemistry, grain structure, and hence the oxygen inward flux within continuous alumina itself are expected to play a minor role and were, therefore, not elucidated. The integration of Ta into protective oxides was shown to affect its transport properties and growth rates. For alumina-forming Ni-base superalloys, a substantial Ta-enrichment along the oxide grain boundaries could be demonstrated based on TEM investigations [65]. The latter was suggested to block the transport of cations within the grain boundaries, in analogy to the reactive element effect [65].

Overall, the results indicate that W and Ta have a strong impact on the oxidation performance of superalloys. However, neither supply nor activity considerations alone are sufficient to explain the effect of refractory metal concentrations on the oxidation resistance. We conclude that accelerated outward diffusion of Al, Cr, and Si contributes to the enhanced formation of continuous protective scales in case of the W derivatives. In the case of the Ta derivatives, such supply considerations do not hold. Instead, increased activities of Al, Cr, and Si but also secondary oxygen gettering by Ta (as described for the third element effect) are expected to increase the oxidation resistance. Overall, even more promising oxidation properties for alloys with high Co levels might be achievable in the high-temperature regime, if the refractory metal content is further balanced, e.g., by using material library approaches.

Summary and Conclusions

The high-temperature oxidation behavior of 6 single-crystalline γ/γ'-strengthened Co/Ni-based superalloys was elucidated at 1050 °C and 1150 °C for exposure durations of 100 h and compared to the commercial Ni-base superalloys CMSX-4. Three superalloys, ERBOCo-1, ERBOCo-1-W, ERBOCo-1+Ta are Co-based (Co/Ni ratio: 1.4) and the others ERBOCo-1X, ERBOCo-1X-W, ERBOCo-1X+Ta are Ni-based (Co/Ni ratio: 0.7). The nominal content of the alloying elements Al, Cr, Ti, Si, and Hf remained nominally unaltered for all alloys, whereas the W and Ta contents were varied by 40% compared to the original systems. Results from time resolved thermogravimetry, cross sections, thermodynamic calculations, and diffusion couple experiments lead to the following conclusions:

- Both increasing the Ta and reducing the W content improve the oxidation resistance, as continuous alumina scale growth is facilitated compared to the original alloys ERBOCo-1 and ERBOCo-1X. Despite a massive improvement, the deriv-

atives cannot outperform CMSX-4 in terms of oxidation resistance. Nevertheless, considering the high Co levels of all alloys, the improvements are considerable.

- Thermodynamic calculations indicate that the Al, Cr, and Si activities are increased in the case of the Ta derivatives, even though the nominal content of the protective scale formers was kept constant. In contrast, a reduction of the W content leads to lower activity values. Overall, the activity results do not reflect the order regarding the oxidation resistance of the 6 alloys.
- For the Co-base derivatives—ERBOCo-1, ERBOCo-1-W, and ERBOCo-1 + Ta—diffusion couple experiments were performed to qualitatively assess the availability of protective scale formers (Al, Cr, and Si) as a function of the refractory metal content. In the case of the W derivative (3 at.% W instead of 5 at.%), enhanced transport rates of these elements were found, which coincides with the improved oxidation resistance according to the Wagner criterion. In case of the Ta derivative (2.1 at.% Ta instead of 1.5 at.%), no increased transport rates of protective scale formers were found. Overall, also the diffusion results do not reflect the order regarding the oxidation resistance.
- We conclude that the improvement in oxidation resistance in the case of the W derivatives is due to the accelerated outward diffusion of Al and Cr enabling the fast formation of continuous protective scales. In the case of the Ta derivatives, it is assumed that increased activities of Al and Cr or also the high oxygen affinity of Ta leading to secondary oxygen gettering may induce the improvement.

Appendix

See Figs. 10 and 11.
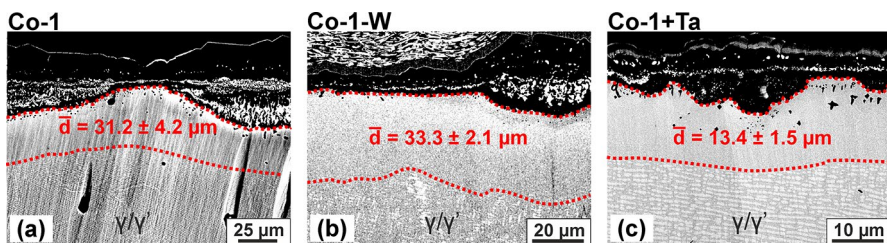
Fig. 10 BSE micrographs of ERBOCo-1 (**a**), ERBOCo-1-W (**b**), and ERBOCo-1 + Ta (**c**) after 100 h oxidation at 1050 °C with high contrast to depict the γ'-depleted zone within the alloy underneath the oxide. The red dashed lines indicate the interfaces of the γ'-depleted zone toward the oxide (upper one) or the two-phase substrate (lower one), respectively. The average thicknesses $\bar{d}$ of the depletion zones are given within the micrographs
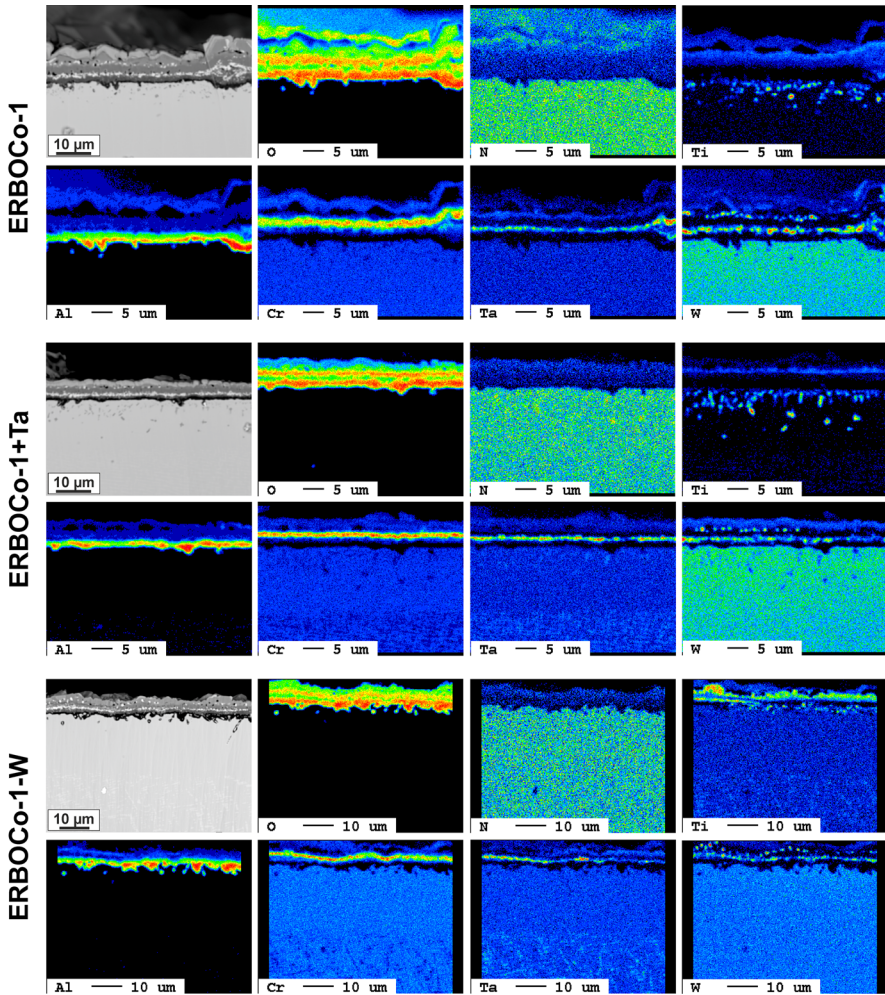
Fig. 11 BSE micrographs together with elemental distribution maps of the thin oxide scales of ERBOCo-1 (top), ERBOCo-1+Ta (middle), and ERBOCo-1-W (bottom) subsequent to 100 h exposure at 1050 °C determined by EPMA

Author Contributions SPH performed the oxidation experiments as well as the microscopic investigations, wrote the initial draft of the manuscript, and prepared all figures. LH supervised the laboratory work as well as the interpretation of the diffusion couple experiments. BW conducted the thermodynamic calculations, facilitated their interpretation, and aided in the conceptualization of the diffusion couple experiments. The students FG and BA conducted parts of the laboratory work as part of their theses, including sample preparation, and cross sectioning. Also, they performed the initial data curation. MW helped to outline the selected approach and corrected the initial manuscript. The input of SN mainly

concerned alloy design and final corrections of the manuscript. CZ enabled the thermodynamic calculation activities and improved the initial manuscript via corrections. SV conceptualized and supervised all research activities and led the formal analyses. All authors reviewed the manuscript. All contributors are stated and have read and agreed to the published version of the manuscript.

Declarations

Conflict of interest On behalf of all authors, the corresponding author states that there is no conflict of interest.

References

1. T. M. Pollock and S. Tin, *Journal of Propulsion and Power* **22**, 2006 (361). https://doi.org/10.2514/1.18239.
2. A. Sato, Y.-L. Chiu, and R. C. Reed, *Acta Materialia* **59**, 2011 (225). https://doi.org/10.1016/j.actamat.2010.09.027.
3. J. L. Smialek and G. H. Meier, *Wiley-Interscience, John Wiley and Sons, Superalloys II-High Temperature Materials for Aerospace and Industrial Power,* 293–326. ISBN: 9780471011477 (1987)
4. K. Kawagishi, H. Harada, A. Sato, A. Sato, and T. Kobayashi, *JOM the journal of the Minerals, Metals & Materials Society* **58**, 2006 (43). https://doi.org/10.1007/s11837-006-0067-z.
5. G. L. Erickson, *JOM.* **47**, 1995 (36). https://doi.org/10.1007/BF03221147.
6. G. E. Fuchs, *Materials Science and Engineering A.* **300**, 2001 (52). https://doi.org/10.1016/S0921-5093(00)01776-7.
7. R. Popp, S. Haas, F. Scherm, et al., *Journal of Alloys and Compounds* **788**, 2019 (67). https://doi.org/10.1016/j.jallcom.2019.01.329.
8. B. Gleeson High-Temperature Corrosion of Metallic Alloys and Coatings. In *Materials Science and Technology: A Comprehensive Treatment*, eds. R. W. Cahn, P. Haasen, E. J. Kramer, eds. pp. 173–228. (2000) https://doi.org/10.1002/9783527619306.ch14
9. R. Darolia, *International Materials Reviews.* **64**, 2018 (1). https://doi.org/10.1080/09506608.2018.1516713.
10. A. Sato, H. Harada, A.-C. Yeh, et al., *Proceedings of the International Symposium on Superalloys.* 2008. https://doi.org/10.7449/2008/Superalloys_2008_131_138.
11. K. Kawagishi, A.-C. Yeh, T. Yokokawa, T. Kobayashi, Y. Koizumi, and H. Harada, *Superalloys* **2012**, 2012 (189). https://doi.org/10.1002/9781118516430.ch21.
12. B. A. Pint, J. R. DiStefano, and I. G. Wright, *Materials Science and Engineering: A.* **415**, 2006 (255). https://doi.org/10.1016/J.MSEA.2005.09.091.
13. J. Sato, T. Omori, K. Oikawa, I. Ohnuma, R. Kainuma, and K. Ishida, *Science* **2006**, (312), 1979 (90). https://doi.org/10.1126/science.1121738.
14. S. Neumeier, L. P. Freund, and M. Göken, *Scr Mater.* **109**, 2015 (104). https://doi.org/10.1016/j.scriptamat.2015.07.030.
15. L. P. Freund, S. Giese, D. Schwimmer, H. W. Höppel, S. Neumeier, and M. Göken, *Journal of Materials Research* **32**, 2017 (4475–4482). https://doi.org/10.1557/jmr.2017.315.

16. S. P. Hagen, M. Weiser, B. Abu-Khousa, and S. Virtanen, *Metallurgical and Materials Transactions A.* 2022. https://doi.org/10.1007/s11661-022-06620-6.

17. K. Shinagawa, T. Omori, J. Sato, et al., *Materials Transactions* **49**, 2008 (1474). https://doi.org/10.2320/matertrans.MER2008073.

18. C. H. Zenk, S. Neumeier, M. Kolb, et al., *Superalloys* **2016**, 2016 (969). https://doi.org/10.1002/9781119075646.ch103.

19. E. A. Lass, D. J. Sauza, D. C. Dunand, and D. N. Seidman, *Acta Materialia.* **147**, 2018 (284). https://doi.org/10.1016/j.actamat.2018.01.034.

20. C. A. Stewart, S. P. Murray, A. Suzuki, T. M. Pollock, and C. G. Levi, *Materials & Design* **189**, 2020 (108445). https://doi.org/10.1016/j.matdes.2019.108445.

21. M. Weiser, M. C. Galetz, R. J. Chater, and S. Virtanen, *Journal of the Electrochemical Society* **167**, 2020 (21504). https://doi.org/10.1149/1945-7111/ab69f7.

22. T. König, S. P. Hagen, S. Virtanen, and M. C. Galetz, *Metallurgical and Materials Transactions A.* **53**, 2022 (4023). https://doi.org/10.1007/s11661-022-06807-x.

23. R. A. Rapp, *Corrosion* **21**, 2013 (382). https://doi.org/10.5006/0010-9312-21.12.382.

24. D. L. Douglass, *Oxidation of Metals.* **44**, 1995 (81). https://doi.org/10.1007/BF01046724.

25. W. Zhao, Y. Kang, J. M. A. Orozco, and B. Gleeson, *Oxidation of Metals.* **83**, 2015 (187). https://doi.org/10.1007/s11085-014-9516-1.

26. H. M. Hindam and W. W. Smeltzer, *Journal of the Electrochemical Society* **127**, 1980 (1622). https://doi.org/10.1149/1.2129964.

27. N. Birks, G. Meier, and F. Pettit, in *Introduction to the High Temperature Oxidation of Metals*, eds. F. S. Pettit, G. H. Meier and N. Birks (Cambridge University Press, Cambridge, 2006), pp. 101–162.

28. C. Wagner, *Zeitschrift für Elektrochemie, Berichte der Bunsengesellschaft für physikalische Chemie.* **63**, 1959 (772). https://doi.org/10.1002/bbpc.19590630713.

29. P. Kofstad, *High Temperature Corrosion*, (Elsevier, New York, 1988), p. 132.

30. R. A. Rapp, *Acta Metallurgica.* **9**, 1961 (730). https://doi.org/10.1016/0001-6160(61)90103-1.

31. R. Pillai, A. Chyrkin, and W. J. Quadakkers, *Oxidation of Metals.* **96**, 2021 (385). https://doi.org/10.1007/s11085-021-10033-y.

32. N. Volz, C. H. Zenk, R. Cherukuri, et al., *Metallurgical and Materials Transactions A.* **49**, 2018 (4099). https://doi.org/10.1007/s11661-018-4705-1.

33. C. H. Zenk, N. Volz, C. Zenk, P. J. Felfer, and S. Neumeier, *Crystals (Basel).* 2020. https://doi.org/10.3390/cryst10111058.

34. S.-J. Park, S.-M. Seo, Y.-S. Yoo, H.-W. Jeong, and H. Jang, *Corrosion Science* **90**, 2015 (305). https://doi.org/10.1016/j.corsci.2014.10.025.

35. X. Lu, S. Tian, X. Yu, and C. Wang, *Rare Metals* **30**, 2011 (439). https://doi.org/10.1007/s12598-011-0320-7.

36. S. Espevik, R. A. Rapp, P. L. Daniel, and J. P. Hirth, *Oxidation of Metals.* **20**, 1983 (37). https://doi.org/10.1007/BF00658126.

37. S. Espevik, R. A. Rapp, P. L. Daniel, and J. P. Hirth, *Oxidation of Metals.* **14**, 1980 (85). https://doi.org/10.1007/BF00603987.

38. D. Kubacka, M. Weiser, and E. Spiecker, *Corrosion Science* **191**, 2021 (109744). https://doi.org/10.1016/J.CORSCI.2021.109744.

39. G.H. Meier, F. S. Pettit and A. S. Khan in *Rapid Solidification Processing, Principles and Technologies III*, ed. R. Mehrabian. (National Bureau of Standards: Gaithersburg, MD, 1982) pp. 348–359

40. F. S. Pettit and G. H. Meier, *Superalloys.* 1984. https://doi.org/10.7449/1984/SUPERALLOYS_1984_651_687.

41. S. Neumeier, H. U. Rehman, J. Neuner, et al., *Acta Materialia* **106**, 2016 (304). https://doi.org/10.1016/J.ACTAMAT.2016.01.028.

42. I. Barin, *Thermochemical data of pure substances*, 3rd ed (Wiley-VCH, New York, NY, 1995)

43. M. Chase, *NIST-JANAF Thermochemical Tables*, 4th Edition, American Inst. of Physics; 1998

44. G. N. Irving, J. Stringer, and D. P. Whittle, *Corrosion Science* **15**, 1975 (337). https://doi.org/10.1016/S0010-938X(75)80015-1.

45. H. T. Mallikarjuna, N. L. Richards, and W. F. Caley, *Journal of Materials Engineering and Performance* **26**, 2017 (2014). https://doi.org/10.1007/s11665-017-2630-x.

46. F. H. Stott, G. C. Wood, and J. Stringer, *Oxidation of Metals.* **44**, 1995 (113). https://doi.org/10.1007/BF01046725.

47. B. H. Kear, F. S. Pettit, D. E. Fornwalt, and L. P. Lemaire, *Oxidation of Metals.* **3**, 1971 (557–569). https://doi.org/10.1007/BF00605003.

48. Y. Niu, S. Wang, F. Gao, Z. Zhang, and F. Gesmundo, *Corrosion Science.* **50**, 2008 (345). https://doi.org/10.1016/j.corsci.2007.06.019.

49. S. P. Hagen High-Temperature Oxidation of Cobalt-Rich Superalloys. Thesis. 2023;45. https://opus4.kobv.de/opus4-fau/frontdoor/index/index/docId/21591

50. S. P. Hagen, M. Weiser, D. Kubacka, E. Spiecker, and S. Virtanen, *Oxidation of Metals.* **94**, 2020 (477). https://doi.org/10.1007/s11085-020-10003-w.

51. M. Weiser, R. J. Chater, B. A. Shollock, and S. Virtanen, *Npj Materials Degradation* **3**, 2019 (33). https://doi.org/10.1038/s41529-019-0096-z.

52. G. Hou, Y. An, X. Zhao, H. Zhou, and J. Chen, *Acta Materialia* **95**, 2015 (164). https://doi.org/10.1016/j.actamat.2015.05.025.

53. M. Bensch, C. H. Konrad, E. Fleischmann, C. M. F. Rae, and U. Glatzel, *Materials Science and Engineering A.* **577**, 2013 (179). https://doi.org/10.1016/j.msea.2013.04.032.

54. G. Brewster, I. M. Edmonds, and S. Gray, *Oxidation of Metals.* **81**, 2014 (345). https://doi.org/10.1007/s11085-013-9440-9.

55. D. Yun, S.-M. Seo, H. Jeong, and Y. Yoo, *Journal of Alloys and Compounds.* 2017. https://doi.org/10.1016/j.jallcom.2017.03.179.

56. S. W. Yang, *Oxidation of Metals.* **15**, 1981 (375). https://doi.org/10.1007/BF00603531.

57. T. Galiullin, A. Chyrkin, R. Pillai, R. Vassen, and W. J. Quadakkers, *Surface and Coatings Technology* **350**, 2018 (359). https://doi.org/10.1016/j.surfcoat.2018.07.020.

58. W. H. Blades, E. J. Opila, and K. Sieradzki, *Journal of the Electrochemical Society* **169**, 2022 (61501). https://doi.org/10.1149/1945-7111/ac751f.

59. B. Gorr, F. Mueller, H.-J. Christ, et al., *Journal of Alloys and Compounds* **688**, 2016 (468). https://doi.org/10.1016/j.jallcom.2016.07.219.

60. L. Qin, D. Kubacka, E. Spiecker, R. Drautz, and J. Rogal, *Physical Review Materials* **7**, 2023 (13403). https://doi.org/10.1103/PhysRevMaterials.7.013403.

61. M. Weiser and S. Virtanen, *Oxidation of Metals.* **92**, 2019 (541). https://doi.org/10.1007/s11085-019-09934-w.

62. A. Jalowicka, W. Nowak, D. Naumenko, L. Singheiser, and W. J. Quadakkers, *Materials and Corrosion.* **65**, 2014 (178). https://doi.org/10.1002/maco.201307299.

63. K. Wollgarten, T. Galiullin, W. J. Nowak, W. J. Quadakkers, and D. Naumenko, *Corrosion Science* **173**, 2020 (108774). https://doi.org/10.1016/j.corsci.2020.108774.

64. W. J. Nowak, B. Wierzba, and J. Sieniawski, *High Temperature Materials and Processes.* 2018. https://doi.org/10.1515/htmp-2017-0089.

65. J. Wang, M. Chen, S. Zhu, and F. Wang, *Applied Surface Science* **345**, 2015 (194–203). https://doi.org/10.1016/j.apsusc.2015.03.157.

Authors and Affiliations

S. P. Hagen[1] · L. Haussmann[2] · B. Wahlmann[3] · F. Gebhardt[1] · B. Abu-Khousa[1] · M. Weiser[2] · S. Neumeier[2] · C. Zenk[3] · Sannakaisa Virtanen[1]

✉ Sannakaisa Virtanen
virtanen@ww.uni-erlangen.de

S. P. Hagen
sebastian.p.hagen@fau.de

L. Haussmann
lukas.haussmann@fau.de

B. Wahlmann
benjamin.wahlmann@fau.de

F. Gebhardt
florian.gebhardt@studium.uni-erlangen.de

B. Abu-Khousa
abukhousa.baraa@gmx.de

M. Weiser
martin.weiser@fau.de

S. Neumeier
steffen.neumeier@fau.de

C. Zenk
christopher.zenk@fau.de

[1]   Department of Materials Science and Engineering, Institute IV: Surface Science and Corrosion
      (LKO), Friedrich-Alexander-Universität Erlangen-Nürnberg, 91058 Erlangen, Germany

[2]   Department of Materials Science and Engineering, Institute I: General Materials Properties, Frie
      drich-Alexander-Universität Erlangen-Nürnberg, 91058 Erlangen, Germany

[3]   Department of Materials Science and Engineering, Institute II: Materials Science
      and Engineering for Metals (WTM), Friedrich-Alexander-Universität Erlangen-Nürnberg,
      91058 Erlangen, Germany